Multiple resonances in lossy acoustic black holes - theory and experiment

Olga Umnova [a,*], Daniel Brooke [a], Philippe Leclaire [b], Thomas Dupont [c]

[a] *University of Salford, Manchester, England, UK*
[b] *DRIVE – ISAT Universitie de Bourgogne, Nevers, France*
[c] *Department of Mechanical Engineering, École de Technologie Supérieure, Montréal, Québec, Canada*

A B S T R A C T

Acoustic properties of the metamaterial graded absorber, also known as ``acoustic black hole'', are studied in the linear regime. The absorber consists of thin metallic circular plates, each with a central perforation, separated by annular air cavities. Radius of the perforation in each plate is gradually decreasing with the distance from the plate to the front surface, forming a central channel with a staircase radius profile. A semi-analytical equivalent fluid model accounting for the variations of both the effective density and compressibility of air inside this channel is developed, which incorporates the staircase variations of the perforation radius with distance and assumes motionless plates. The viscous and thermal losses inside the side cavities and the central channel are accounted for using a well-established Johnson-Champoux-Allard-Lafarge model. It is demonstrated that high absorption coefficient values are achieved in a wide range of frequencies starting from a few hundred Hz or less. At low frequencies, the resonances along the length of the structure, i.e. global resonances, are responsible for sound attenuation. At higher frequencies, the resonances of the lateral cavities, i.e. local resonances, play a major role. The upper boundary of the frequency range of high sound absorption is determined by the resonance frequency of the front annular plate. The model is validated against impedance tube measurements on five samples of different geometry and FEM models. FEM model predicts that the elasticity of the plates affects the absorption coefficient behaviour in the frequency range of plate resonances and at frequencies well below the plate resonances.

1. Introduction

Acoustic metamaterials with graded properties have attracted a significant amount of attention in the last decade. The investigation of the sound retarding structures, such as ``acoustic black holes'' (ABH) has been started in pioneering works by Mironov and Pislyakov [1] and Krylov [2]. Air-borne acoustic black hole introduced in [1] must be distinguished from solid-borne acoustic black holes developed in [2]. A large body of the literature has been devoted to the latter and has been summarised in a recent review [3]. The present paper deals with air-borne acoustic black hole and is greatly inspired by the work [1].

The structure studied in [1] comprised a series of plates with constant outer radius and with a central perforation whose radius gradually decreased from the front to the back of the sample. The air cavities between the plates resulted in the admittance of the

---

perforation walls, varying along the sample length in accordance with the perforation radius variations. The effect of this was a gradual decrease of the wave speed through the structure leading, eventually, to elimination of reflections of the incident wave. Only the frequencies below the resonances of the lateral cavities were considered. Continuous variations of the central perforation radius were assumed in the model to approximate the discrete structure. In the following works by El Ouahabi et al. [4,5] the ABH structures with linear and quadratic dependence of the inner radius on the distance have been studied experimentally. A reduction of the reflection coefficient was demonstrated in general agreement with the predictions of [1]. In the recent work by Mironov and Pislyakov [6] the results of analytical model developed in [1] were directly compared with the measurements. It was found that the continuous model is not accurate enough for the description of the discrete structure, hence effective length was introduced as an adjustable parameter to obtain the agreement between the measurements and the predictions.

To overcome the limitations of the continuous model, the transfer matrix model (TMM) has been used to calculate the reflection coefficient of the ABH in [7]. In that work, also a parametric study has been performed investigating among others the effects of plate thickness and plate separation on the reflection coefficient. Moreover, the use of TMM has been validated, showing its consistency with the solution of the continuous problem in [8]. In [9], the TMM was used to predict a simultaneous reduction of reflection and transmission of ABH without rigid termination.

In [10] an alternative approach has been developed, whereby the ABH has been replaced by an equivalent fractional order boundary conditions and fractional order elements.

In most works, the intrinsic losses inside the main perforation and the cavities between the plates have been accounted for by simply introducing a small imaginary part to sound speed. When an additional sound absorbing material was added in the form of porous layers as in [7] or perforated plates as in [11], then the standard models were used to account for their losses. In the second part of [6], an equivalent fluid approach has been adapted to model the ABH with effective density varying along the length of the structure due to added layers of various materials e.g., felt. In this case the radius of the duct was kept constant, but the black hole effect was still achieved.

However, viscous and thermal losses in the main perforation and in the side-cavities are frequency dependent and also dependent on the spacing between the plates and the radius of the main perforation. These effects were considered in [12] within the framework of TMM. The structures studied in [12] comprised the main channel loaded by the side Helmholtz resonators with dimensions of both channel and resonators varying along the sample depth. It has been shown that nearly perfect absorption can be achieved in a relatively wide range of frequencies due to resonances of the slightly mistuned Helmholtz resonators. In that study, a thin structure of sub-wavelength length was considered, which differs from the main body of works on air-borne ABH absorbers.

A detailed consideration of losses in conventional ABHs has been offered in recent works [13,14]. In both papers the role of resonances of the side-cavities has been mentioned. In [13] an outer tube has been identified as the main source of damping and high localised pressure amplitudes in resonating cavities have been obtained. It was suggested that the small amount of sound absorbing material should, for this reason, be added at the end of each cavity, and not at the end of the waveguide as was done in [4,5]. In [14] a numerical solution of governing equations has been performed using FEM and accounting for viscous and thermal losses at the boundaries of rigid plates and air. The dips in the reflection coefficient were shown to be at the resonance frequencies of the side-cavities. The numerical results accounting for viscous and thermal losses were compared with a simpler description based on Helmholtz equation with complex sound speed and the shortcomings of the latter have been demonstrated.

It is mentioned in [14], that the description of the ABH based on Helmholtz equation with the complex valued sound speed could be refined ``employing the concept of homogenisation and equivalent fluid''. An equivalent fluid approach has advantages over the TMM and purely numerical description such as FEM. Its formulation, requiring two effective quantities, is compact and gives a clear insight into the governing physics. It is universal and can be applied to various systems with subwavelength size inhomogeneities e.g., porous materials and metamaterials. Contrary to TMM, it can be relatively easily generalised to include nonlinear effects, which are important at high levels of acoustic excitation [15].

An equivalent fluid model for the ABH absorber and its validation is the main subject of the current work. A graded structure studied here is a similar design to the ABH from [1]. However, the width of the side cavities is small enough for the viscous and thermal losses to be important for low and medium frequencies (few hundred Hz of less). Also, the radius of the main perforation decreases to the values comparable to the width of these cavities or, in some samples, becomes even smaller. The losses in the boundary layers in both the main perforation and side cavities are accounted for using Johnson - Champoux – Allard - Lafarge (JCAL) equivalent fluid model [16]. The aim is to develop an equivalent fluid model similar to that descried in our earlier work [15] but at the same time to account for the gradual decrease of the central perforation radius along the length of the absorber. The latter leads to both the variations of the admittance of the side-cavities (this was considered in [1]) and to the gradual increase of viscous and thermal losses in the central perforation. The thermal losses in the main perforation and the presence of the side cavities modify the effective compressibility of fluid in the perforation, as was shown in [15]. The viscous losses in the central perforation affect effective density of air in it. So, in the model presented in this work, the gradual variations of both the effective compressibility of the equivalent fluid inside the central perforation and its effective density are considered. The working frequency range covers the resonances of the side cavities. Similar to [12], the cavities between the plates act as side loaded mistuned (due to variations in their inner radii along the sample length) resonators. Although our description is not based on TMM, the staircase variations of the central perforation radius due to discrete nature of the design are accounted for in the continuous equivalent fluid model.

The rest of the paper is organised as follows. In Section 2 the equivalent fluid model is formulated. First, wave equation for pressure in the waveguide with varying cross section and position dependent dynamic density and compressibility is derived, followed by the equation for the input admittance of the hard backed ABH absorber. In Section 3 the predictions of the semi-analytical model are discussed. We consider these for five samples used in the experiments. The samples represent two different geometries of the central

perforation profile -linear decrease of its radius and horn type profiles. Also, the samples are of different lengths and have different widths of the side cavities. In Section 4, the model is validated by comparing its predictions with both the FEM calculations and impedance tube measurements. The FEM model does not use the equivalent fluid assumption and instead computes sound propagation in the thermo-viscous fluid (air) constrained within a set of rigid boundaries (plates), as was also done in [14]. In Section 5, the effect of plate elasticity on the results is investigated using an FEM model which accounts for fluid-structure interactions. This is done because the resonance frequencies of some annular plates fall within the working frequency range of the ABH. Lastly, the main results and possible directions for future work are summarised in the Conclusions.

2. Equivalent fluid model

We consider a structure, similar to that described in [1], i.e., a cylindrical absorber of radius R consisting of motionless rigid plates, each with a central orifice, separated by air cavities. The orifice size decreases from the front to the back surface of the structure. The surface area of the perforation is described by a function $S(x) = \pi r(x)^2$, where x measures the depth, with a front surface being at $x = 0$. The front and side view of the structure is shown in Fig. 1a,b. In Fig. 1b, all dimensions are labelled.

The purpose of this section is to derive an equation for the surface admittance of this sample accounting for the variations of the effective density $\rho(x)$ and effective compressibility $C(x)$ of the equivalent fluid in the perforation loaded by the lateral cavities along the sample depth x. Decrease of the central perforation radius leads to increase of viscous losses, described by position dependent effective density. Effective compressibility of air in the main perforation is affected by both the size of the main perforation and the admittance of its walls which is nonzero due to the presence of the lateral cavities. This is described by Eq. (6) in reference [15]. Varying the central perforation size affects both contributions to the effective compressibility. We consider the propagating wave to be plane. The frequency of the wave is such that wavelength is much larger than the widest part of the channel, $f \ll \frac{c_0}{R}$.

We start with equation (14.7.1) from [17] relating condensation $s = \rho/\rho(x)$ and acoustic displacement ζ in the channel with varying cross section area $S(x)$:

$$\frac{\rho}{\rho(x)} = -\frac{1}{S(x)}(S(x)\zeta)^{'}.$$

(1)

Prime stands for the derivative with respect to distance x. Relationship between acoustic pressure and density variations of air, p
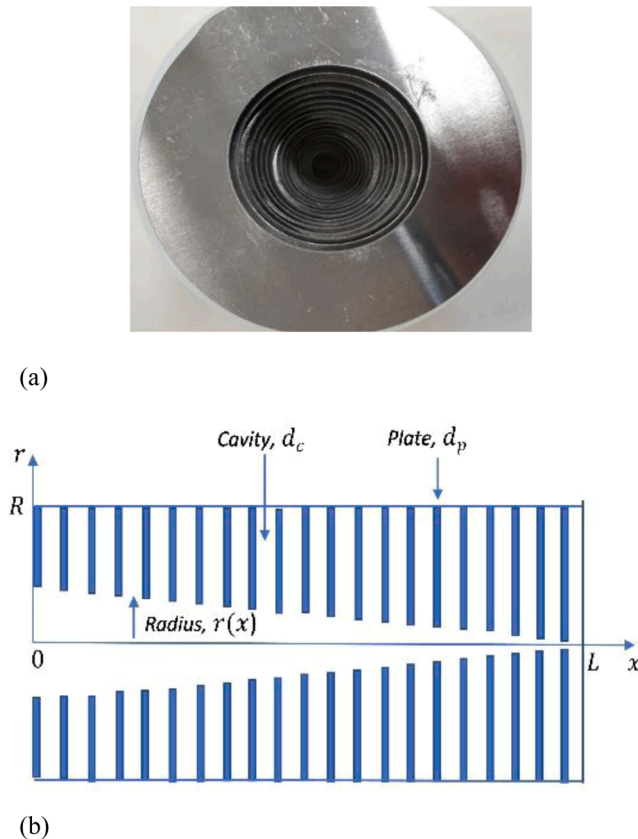

(a)

(b)

Fig. 1. Front (a) and side (b) views of the absorber comprised metallic plates separated by air cavities.

and ρ, is given by the equation of state (similar to equation 5.2.6 in [17])

$$p = c^2(x)\rho,$$

(2)

where $c(x) = (C(x)\rho(x))^{-\frac{1}{2}}$ is complex wave speed in the perforation. This transforms Eq. (1) into

$$\frac{p}{\rho(x)c^2(x)} = -\frac{1}{S(x)}(S(x)\zeta)'.$$

(1a)

The next step is to obtain relationship between the displacement ζ and pressure variation p. Here and in the following, time dependence in the form $e^{-i\omega t}$ is adopted. Combining Euler's equation (see (5.4.10) in [17])

$$-i\omega\rho(x)v = -p'$$

(3)

and relationship between particle velocity v and displacement ζ, $v = \frac{d\zeta}{dt}$, for a harmonic wave

$$v = -i\omega\zeta,$$

(4)

a relationship between the displacement and pressure is obtained:

$$\zeta = \frac{p'}{\omega^2\rho(x)}.$$

(5)

Substituting this in (1'), equation for pressure p is derived

$$\frac{p}{\rho(x)c^2(x)} = -\frac{1}{S(x)}\left(S(x)\frac{p'}{\omega^2\rho(x)}\right)'.$$

(6)

Expanding the derivative on the right-hand side of (6), the final equation for the pressure in the perforation with the varying cross-sectional area is obtained:

$$p'' + p'\left(\frac{S'(x)}{S(x)} - \frac{\rho'(x)}{\rho(x)}\right) + k^2(x)p = 0,$$

(7)

where $k(x) = \omega/c(x) = \omega(C(x)\rho(x))^{\frac{1}{2}}$ is position x dependent wavenumber. Equation (7) is reduced to the usual Webster equation if $k(x) = k_0 = \omega/c_0$ and $\rho(x) = \rho_0$, where ρ_0 is equilibrium density of air and c_0 is sound speed in air.

This equation also coincides with Eq. (4) from [1] if the losses in the perforation are not considered. Indeed, in this case $\rho'(x) = 0$ as the effective density remains equal to that of air $\rho(x) = \rho_0$. Then, equation for effective compressibility is similar to Eq. (6) from [15], $C(x) = C_0(1 + 2iG_w(x)/(k_0r(x)))$, here $C_0 = (\rho_0 c_0^2)^{-1}$ is equilibrium compressibility of air, $G_w(x)$ is position dependent normalised admittance of the perforation wall, having inner radius $r(x)$ and outer radius R. Hence, Eq. (4) from [1] is recovered.

Now, we introduce dimensionless spatial variable $X = x/L$, where L is the length of the sample. In this case the front surface of the absorber corresponds to $X = 0$ and its backing corresponding to the termination point is set to $X = 1$.

Furthermore, a dimensionless wavenumber $q = k_0L$ and a normalised position dependent surface admittance of the absorber is $\Gamma(X) = \phi_p(X)\rho_0 c_0 v/p$ are introduced, with $\phi_p(X) = (r(x)/R)^2$ being a position dependent surface porosity.

Using Eq. (3), a Riccati type equation [18] for the normalised surface admittance of the absorber is derived:

$$\Gamma' = iq\left(C_m(X) - \rho_m(X)\Gamma^2\right).$$

(8)

In Eq. (8) and further in the paper, the effective density $\rho_m(X)$ and effective compressibility $C_m(X)$ of air in the material are normalised by equilibrium density of air ρ_0 and compressibility C_0, respectively. They are related to the effective properties of air in the main perforation as $\rho_m(X) = \rho(X)/(\phi_p(X)\rho_0)$ and $C_m(X) = \phi_p(X)C(X)/C_0$.

Boundary condition for the normalised admittance is imposed on the rigid backing situated at $X = 1$.

$$\Gamma(1) = 0$$

(9)

The reflection coefficient **R** and absorption coefficient α for sound wave impinging normally on the surface can be found as

$$\mathbf{R} = \frac{1 - \Gamma(0)}{1 + \Gamma(0)}, \ \alpha = 1 - |\mathbf{R}|^2.$$

(10)

To complete the formulation of the problem a radius profile $r(X)$ and dependences $C_m(X)$ and $\rho_m(X)$ are required. If the radius of the central perforation exceeds the width of the lateral cavities, $r(X) > d_c$, the effect of the latter is described introducing surface admittance of the perforation walls. This, as has been already explained, influences effective compressibility of air in the perforation and not its effective density. This result has been derived in our earlier work [19], in [20] and also follows from classical work by Tidjeman [21]. It is also noted in [19] that expression relating compressibility of air in the perforation and surface admittance of the pore walls is equivalent to introduction of the pressure diffusion function [22]. By performing flow resistivity measurements, it has

been experimentally proven in [15] hat it is not affected by the presence of the lateral cavities when the central perforation diameter was 4/3 of the cavity width and larger. Flow resistivity is the key parameter defining effective density in the low frequency range. In the black hole absorber, the central perforation radius decreases considerably along the length reaching, close to the backing, the values smaller than the lateral cavities' width. When this happens, description of the effect of cavities by introducing the surface admittance of the perforation wall is, strictly speaking, incorrect. Strong interaction between the neighbouring cavities happening in a confined geometry require treatment using the full scattering model as was done in [20]. In that work the comparisons between the equivalent fluid model and full scattering model are presented. It was, however, demonstrated, that although the predictions of the full scattering model are closer to the data, the equivalent fluid model also provides a good agreement in the low frequency range (see Fig. 6 in [20]). It is thus assumed in the current work, that the effective density of air in the central perforation is not influenced by the presence of the lateral cavities, while the effective compressibility is modified due to non-zero admittance of the perforation walls. Although we accept that this assumption might introduce an error into the model, the comparisons with FEM model presented in Section 4 confirm its validity. Using JCAL model for a cylindrical orifice, the effective density of air $\rho(X)$ is described in terms of position dependent flow resistivity $\sigma(X) = 8\eta/r^2(X)$, characteristic viscous length $\Lambda(X) = r(X)$ and the tortuosity of the straight orifice $\alpha_\infty = 1$. This results in the following expression for the normalised density $\rho_m(X)$

$$\rho_m(X) = \frac{R^2}{r^2(X)} \left(1 + \frac{8\eta}{-i\omega\rho_0 r^2(X)} \sqrt{1 + \frac{-i\omega}{\omega_b(X)}} \right) \tag{11}$$

A position dependent Biot frequency $\omega_b(X)$ is introduced here, which is equal to $\omega_b(X) = \sigma^2(X)\Lambda^2(X)/(4\rho_0\eta\alpha_\infty^2)$, where η is viscosity of air, Λ characteristic viscous length, α_∞ is tortuosity. For a straight cylindrical orifice with varying radius $r(X)$, this is equal to $\omega_b(X) = 16\eta/(r^2(X)\rho_0)$. Effects of inertia dominate over viscosity effects, i.e., viscous boundary layer is much smaller than the smallest dimension, in the frequency range $\omega \gg \omega_b$. In this study, the minimum value of the orifice radius is $r(1) = 0.5$ mm in samples 4–5 and $r(1) = 1$ mm in samples 1–3. This gives $\omega_b(1) = 960$ Rad s^{-1} for samples 4–5 and $\omega_b(1) = 240$ Rad s^{-1}. Dimensions of the samples are shown in Table 1. This means that in the measurement range of frequencies 100 Hz- 1700 Hz, $\omega/\omega_b(X) \gg 1$ for samples 1–3. This allows simplification of the expression for the effective material density, which is used for calculations

$$\rho_m(X) \approx \frac{R^2}{r^2(X)} \left(1 + 2\sqrt{\frac{\eta}{-i\omega\rho_0}} \frac{1}{r(X)} \right) \tag{12}$$

The normalised effective compressibility $C_m(X)$ is given by Eq. (6) from [3] with normalisation applied

$$C_m(X) = \left(C_p(X) + \frac{iG_w(X)}{2k_0 r(X)} \right) \frac{r^2(X)}{R^2} \tag{13}$$

where $G_w(X)$ is the normalised, varying along the sample length, admittance of the central perforation wall. To obtain expression for the normalised effective compressibility of air in the straight cylindrical channel with hard walls C_p, we use JCAL model with the following expressions for thermal permeability and characteristic thermal length $\kappa'(X) = r^2(X)/8$ and $\Lambda' = r(X)$. This gives

$$C_p(X) = \gamma - \frac{\gamma - 1}{1 + \frac{8\eta}{-i\omega N_{pr} r^2(X)} \sqrt{1 + \frac{-i\omega N_{pr}}{\omega_b'}}}, \tag{14}$$

where N_{pr} is Prandtl number and γ is adiabatic constant. The frequencies of interest are higher than Biot thermal frequency $\omega_b'(X) = 16\eta /(r^2(X)\rho_0)$ for samples 1–3, which means that thermal boundary layer is smaller than the cylindrical channel radius. This allows approximation of the effective compressibility of air in the central orifice, which is used in calculations

$$C_p(X) \approx \gamma - \frac{\gamma - 1}{1 + 2\sqrt{\frac{\eta}{-i\omega N_{pr}\rho_0}} \frac{1}{r(X)}} \tag{15}$$

Table 1
Dimensions of the samples.

Samples	Plate thicknessd_p (mm)	Cavity widthd_c (mm)	Smallest perforation radiusr_{min}(mm)	Front perforation radiusr_{max} (mm)	Outer sample radius$R$ (mm)	Sample length$L$ (mm)
Sample 1	1	3	1	25	50	100
Sample 2	1	3	1	15	50	60
Sample 3	1	2	1	25	50	75
Sample 4	1	3	0.5	25	50	100
Sample 5	1	2	0.5	25	50	75

The expression for the normalised admittance $G_w(X)$ has been derived in [15] and is given by Eq. (11) from that paper. Combined with the dependence of the radius $r(X)$, this results in

$$G_w(X) = \frac{i \phi_w \rho_0 c}{Z_c} \frac{J_1(k_c r(X)) - FH_1(k_c r(X))}{J_0(k_c r(X)) - FH_0(k_c r(X))} \qquad (16)$$

Here $F = J_1(k_c R)/H_1(k_c R)$, $J_{0,1}(x)$ and $H_{0,1}(x)$ are Bessel functions of the first kind and Hankel functions, respectively. $\phi_w = d_c/(d_c + d_p)$ is the porosity of the perforation wall, with d_c and d_p being the cavity width and plate thickness, respectively. Wavenumber k_c and the characteristic impedance of air Z_c in the cavity between the plates are calculated using expressions for its normalised effective density ρ_c and effective compressibility C_c, i.e. $k_c = k_0 \sqrt{\rho_c C_c}$, $Z_c = \rho_0 c_0 \sqrt{\rho_c/C_c}$. If the spacing between the plates d_c does not vary, the effective properties of air in the cavities are independent on X.

Using Eq. (19) from [15] for approximation of the admittance of the pore wall below the resonance frequencies of the cavities and assuming that the thermal boundary layer is less than the smallest central perforation radius, the expression for the normalised complex compressibility of air in the perforation is derived:

$$C(X) = \left(1 + \frac{2(\gamma - 1)}{r(X)} \sqrt{\frac{\eta}{-i\omega N_{pr}\rho_0}}\right) + \phi_w C_c \left(\left(\frac{R}{r(X)}\right)^2 - 1\right), \qquad (17)$$

Note, that the dependence of the wall admittance on $r(X)$ in this equation coincides with that of Eq. (5) from [1]. However, in this expression we account for thermal losses in both central perforation (first term in Eq. (17)) and in the lateral cavities (C_c in the second term). An extra dependence on $r(X)$ resulting from effective compressibility of air in the central perforation is also accounted here. In the range of frequencies which includes cavity resonances, the full equations (13), (14) and (16) are used to calculate $C_m(X)$. Expressions for the effective properties of air in the lateral cavities are given in [15] and are reproduced here for completeness. Again, the JCAL model is used, this time for a slit geometry. This results in the following expression for the effective density

$$\rho_c = 1 + \frac{12\eta}{-i\omega\rho_0 d_c^2} \sqrt{1 + \frac{-i\omega}{\omega_b}} \qquad (18)$$

where Biot frequency is $\omega_b = 36\eta\rho_0/d_c^2$. For $d_c = 1$mm and larger, inertial regime is achieved in the whole working range of frequencies, so high frequency approximation can be used in calculations

$$\rho_c(\omega \gg \omega_b) \approx 1 + 2\sqrt{\frac{\eta}{-i\omega\rho_0}} \frac{1}{d_c} \qquad (19)$$

Effective compressibility of air in the slit is described as

$$C_c = \gamma - \frac{\gamma - 1}{1 + \frac{12\eta}{-i\omega N_{pr} d_c^2} \sqrt{1 + \frac{-i\omega}{\omega_b'}}} \qquad (20)$$

where thermal Biot frequency is $\omega_b' = \omega_b$. Again, a high frequency approximation is valid in the whole working range of frequencies, that is

$$C_c(\omega \gg \omega_b') \approx \gamma - \frac{\gamma - 1}{1 + 2\sqrt{\frac{\eta}{-i\omega N_{pr}\rho_0}} \frac{1}{d_c}} \qquad (21)$$

To conclude, the surface admittance of the absorber is calculated using Eq. (8) with the boundary condition (9) set at the rigid termination. This equation is complemented by the position dependent effective properties of the material. Effective density $\rho_m(X)$ is described by Eq. (11) or approximation (12) which is valid in the inertial regime. According to equation (13), the effective compressibility $C_m(X)$ depends on that of the cylindrical pore C_p Eq. (14) and approximation ((15)) and on the admittance of the wall $G_w(X)$ Eq. (16)). Equation (16) requires the knowledge of the effective properties of air in the lateral cavities, ρ_c and C_c. These are given by Eqs. (19) and ((21).

The limitations of the model presented in this section are the following:

1. Plane wave approximation is valid when $f < \frac{c_0}{2R} = 1700$ Hz.
2. Equivalent fluid model is valid if the wavelength is larger than the period of the structure. For propagation in air this gives $f \ll \frac{c_0}{d_p + d_c} \approx 86$kHz. However, when sound travels inside the central perforation, its speed is greatly reduced. At low frequencies the speed is at its lowest closer to the backing (see Figs. 6). At higher frequencies, the wave practically stops at the location of the resonating cavity (Fig. 7). Inequality $f \ll \frac{c_{local}}{d_p + d_c}$ is thus required to be satisfied, where c_{local} is the local speed of sound at a particular location inside the perforation at frequency f.
3. The use of the wall admittance requires scale separation between the side cavities and the main perforation dimensions, i.e. $r(x) \ll d_c$. This assumption is valid for most locations along the sample length, but not close to the backing where the radius of the perforation can reach values smaller than cavity width d_c.
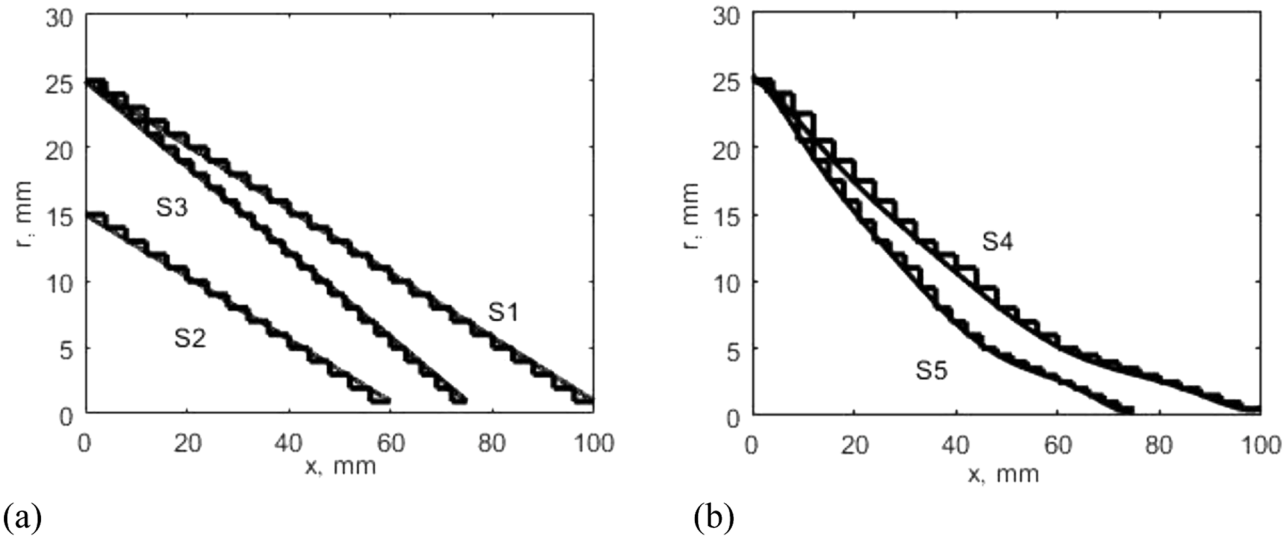
Fig. 2. a) The continuous (22) and staircase (23) approximations of central perforation radius variations $r(x)$, along the sample length, linear profiles. b) The continuous and staircase approximation (24) of central perforation radius variations $r(x)$ along the sample length, horn type profiles. Continuous profiles are approximated by 7th degree polynomials. The x – axis represents the distance from the front surface of the absorber.
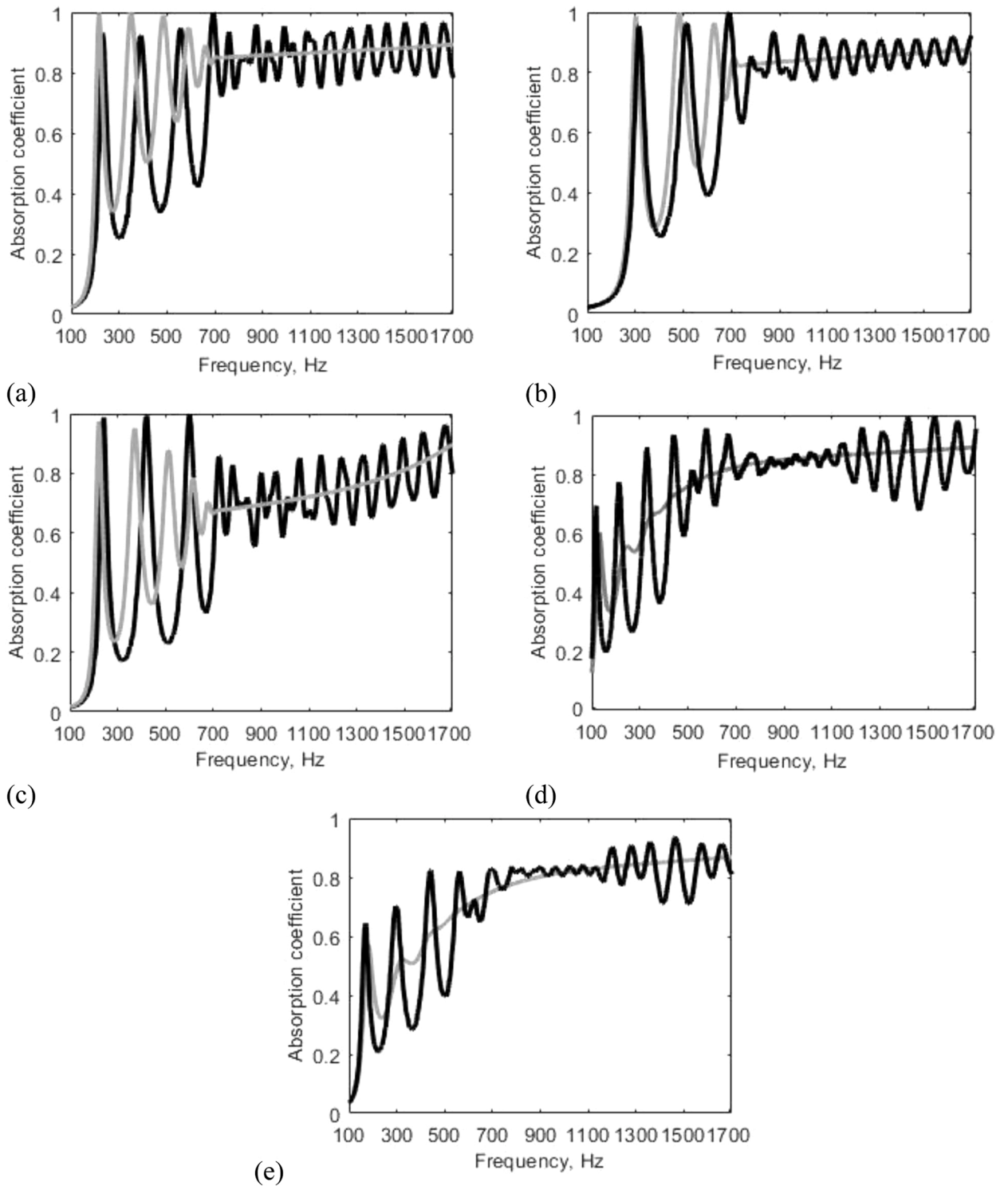
Fig. 3. Calculated absorption coefficient dependence on frequency for linear profile samples 1–3 (a,b,c) and horn profiles 4–5 (d,e). Grey lines – calculations assuming continuous $r(X)$, black lines – calculations with staircase profile approximations (23) and (24).

3. Predictions of the equivalent fluid model

3.1. Description of the samples

The model is now applied to predict the acoustical properties of five samples, used in experiments, as described in Section 3. The graded structures built for the experiments consist of aluminium plates, each plate having a different radius of the central perforation.

The plates have thickness $d_p = 1$ mm and are separated by cavities of width $d_c = 3$ mm (samples 1, 2, 4) and $d_c = 2$ mm (samples 3, 5). The smallest radius of the perforation is $r_{min} = 1$ mm (samples 1, 2,3) and $r_{min} = 0.5$ mm (samples, 4, 5). Samples 1, 3, 4, 5 have a front perforation with $r(0) = 25$ mm and Sample 2 has a smaller front surface perforation with radius $r(0) = 15$ mm. The outer samples' radius is $R = 50$ mm and is equal to the radius of the impedance tube used for the experiments. The dimensions of the samples are summarised in Table 1.

Sample 1 comprises $N = 25$ plates and has a length $L = 100$ mm. Sample 2 comprises $N = 15$ plates and differs in length by 40 mm from Sample 1, thus length of Sample 2 is $L = 60$ mm. The samples are rigidly backed, and the backing is preceded by a cavity. The perforation radius profile $r(x)$ is linear for samples 1–3. For samples 4–5 the radius $r(x)$ decrease following a polynomial dependence on the distance x from the front surface. These profiles are called ``horn type'' in the following. They are used in measurements and simulations to illustrate the dependence of the absorption coefficient behaviour on the function $r(x)$. The variations of radius $r(x)$ for all five samples are shown in Fig. 2,(a-b).

3.2. Absorption coefficient results for continuous and staircase profiles of the central perforation

The central perforation radius dependence on the normalised distance X, $r(X)$, is first approximated by smooth functions preserving the radius of the perforation at the front and back faces, as shown in Fig. 2. For instance, for the linear profiles (Fig. 2,(a)) the following is used

$$r_{cont}(X) = r_{max} - X\frac{r_{max} - r_{min}}{1 - \frac{d_c + d_p}{L}} \tag{22}$$

This gives $r(0) = r_{max}$ and at the position of the last plate $X = 1 - (d_c + d_p)/L$ the radius of the pore is $r(1 - (d_c + d_p)/L) = r_{min}$. For the horn type profiles (Fig. 2,(b)), 7th degree polynomials are used for $r_{cont}(X)$. However, for the samples constructed from the plates, the variations of the main perforation radius are not smooth. For linear profiles (Fig. 2,(a)) they are approximated by the following piecewise function

$$r(X) = r_{min}\left(1 + \sum_{n=1}^{N-1} \Theta\left(1 - X - \frac{d_c + d_p}{L}n\right)\right) \tag{23}$$

where $\Theta(x)$ is Heaviside function.

For two horn type profiles (Fig. 2,(b)) the step of decrease of perforation radius $\Delta r(n) = r(n) - r(n-1)$, (with $r(0) = r_{min}$) is not equal to r_{min} and instead varies from plate to plate. The following approximation of the radius variation with the distance is used in the calculations

$$r(X) = r_{min} + \sum_{n=1}^{N-1} \Delta r(n)\Theta\left(1 - X - \frac{d_c + d_p}{L}n\right). \tag{24}$$

In Fig. 3(a–e), predictions of the absorption coefficient dependence on frequency for continuous and staircase approximations of the central perforation radius are shown. The calculations have been performed assuming ambient temperature of $25°C$ to match the experimental conditions, ambient pressure varied between $100 - 101$ kPa and relative humidity was $30\% - 40\%$.

It is demonstrated in Fig. 3 that the general trend in absorption coefficient dependence on frequency, i.e. isolated peaks at low frequencies followed by high on average value at higher frequencies, is similar for calculations assuming staircase and continuous profiles of $r(x)$. However, only calculations with the staircase profile predict multiple ``ripples'' at higher frequencies. This is because, the staircase profile resolves individual lateral cavities with decreasing inner radius, while the continuous one does not.

In the following, the behaviour of the absorption coefficient in the lower and higher frequency ranges is described.

3.3. Low frequencies, effect of the central perforation profile on absorption coefficient peaks

Both predictions, with smooth and piecewise approximations of $r(X)$, are reasonably close at low frequencies, where the peaks of the absorption coefficients are due resonances along the sample length. Comparing absorption coefficients of the horn profile and linear profile samples of the same length, i.e. samples 1 and 4 and samples 3 and 5, the conclusion could be made, that the horn like profiles have lower absorption coefficient peaks and at lower frequencies. Although the second observation is indeed due to the difference in profile shape, the first is not. The smallest segment radius (next to the backing of the samples) is 0.5 mm for samples 4 and 5, while it is 1 mm for samples 1 and 3. To have a fair comparison between the samples, in the calculations we increase the radius of the last segment in horn profiles 4 and 5 to 1 mm. The comparisons of the absorption coefficient behaviour of these modified samples with linear profiles of the same length are shown in Fig. 4. This figure illustrates the effect of the central perforation profile only on the
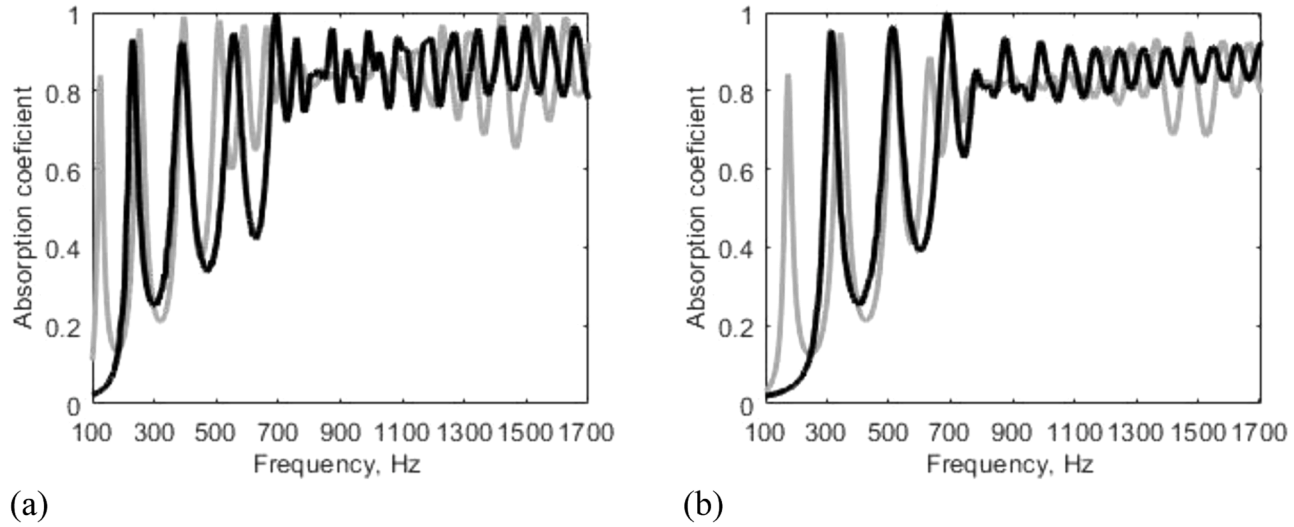
Fig. 4. Effect of the central perforation radius profile $r(X)$ on the absorption coeffcient. a) Linear profile Sample 1 (black) and modified horn type profile of Sample 4 (grey). Both samples are 100 mm length and maximum and minimum central perforation radii are 25 mm and 1 mm. b) Linear profile of Sample 3 (black) and modified profile of Sample 5 (grey). Both samples are 75 mm and max and min central pore radii are 25 mm and 1 mm, respectively.

absorption coefficient dependence on frequency. The radii of the perforation at the front and back surfaces of the samples compared are kept the same. Samples with horn type profiles still possess very low frequency absorption peaks, which are absent for linear profile samples. Indeed, as shown in Fig. 4,(a), a horn profile sample of 100 mm in length has an absorption peak value 0.83 at 124 Hz, whilst the linear profile's first peak has a slightly larger value at 0.93 but at much higher frequency of 229 Hz. In Fig. 4,(b) samples with length 75 mm are compared. The horn profile has an absorption coefficient peak of 0.84 which appears at 177 Hz, while for the linear profile absorption coefficient maximum of 0.95 appears at a much higher frequency 316 Hz. The main reason for this is the lower mean wave speed in the perforation of the horn profile samples. To confirm the last statement, we calculate the wave speed in the perforation $c_m(X) = Re\left((C_m(X)\rho_m(X))^{-\frac{1}{2}}\right)$ along the samples.

The calculated distributions of the wave speeds are shown in Fig. 5 for both the 75 mm long horn type and linear profiles (correspond to Fig. 4,(b)). The frequency is chosen to be 177 Hz which corresponds to the first absorption coefficient peak of the horn type profile. It clearly demonstrates that while the maximum and minimum values of wave speed are the same for two samples, the mean value is lower for horn profile. At 177 Hz mean value of the real part of the normalised wavenumber $\overline{Re(q(X))}$ is 2.57 for the horn type profile, while it is only 1.6 for the linear profile. For the latter, a similar value $\overline{Re(q(X))} = 2.57$ is achieved for a higher frequency $f = 280$ Hz. At the frequency of the linear profile absorption coefficient peak, $f = 316$ Hz, $\overline{Re(q(X))} = 2.93$.

To conclude, at low frequencies the model predicts well resolved absorption coefficient peaks with values close to 1. These peaks are due to resonances along the ABH absorber length or the so called ``quarter wavelength resonances''. For this reason, the frequencies of the peaks are defined by the sound speed inside the perforation. The sound speed variations along the sample length are, in turn, defined by the profile of central perforation radius $r(x)$. So, the value of sound speed averaged along sample length (mean value) is different for different $r(x)$. As demonstrated in Fig. 5, the mean value of sound speed for horn type profile $r(x)$, is lower than for the linear profile. Lower mean sound speed corresponds to shorter (on average) wavelength and consequently lower frequency of the first absorption coefficient peak for a horn type profile (see Fig. 4).

These calculations show that the positions of the absorption peaks at low frequencies could be tuned by changing $r(x)$ profile while keeping the absorber length and maximum and minimum perforation radii, r_{max} and r_{min}, constant. Approximate location of the peaks could be predicted from the calculations of the sound speed value averaged along the sample length and considering ``quarter wavelength resonance'' conditions.

3.4. Higher frequencies, the effect of lateral cavities resonances on the absorption coefficient

At higher frequencies, the results for a staircase profile are clearly affected by the resonances of the individual lateral cavities, which correspond to ``ripples'' in the absorption coefficient dependence on frequency. This is illustrated in Fig. 6,(a) where the absorption coefficient for Sample 1 is plotted together with the absolute values of the admittances of the individual lateral cavities. The latter are calculated using Eq. (16) with the continuous dependence $r(X)$ replaced by the perforation radii of the individual plates. The lowest frequency peak corresponds to the cavity next to sample backing. The resonance frequencies become higher as the cavities get closer to the front of the sample, which is due to an increase of the central perforation radius. Therefore, a continuous smooth approximation of $r(X)$ profile does not resolve the individual cavities, hence the absence of ``ripples''. The absorption coefficient and individual cavity admittances are shown for an extended range of frequencies, up to 3500 Hz. Plane wave approximation is still assumed valid. The Fig. 6 illustrates, that absorption coefficient remains large up towards the resonance frequency of the cavity found
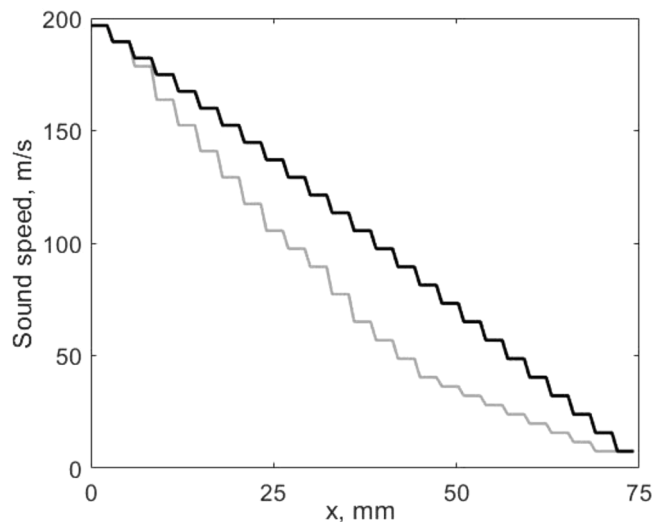

Fig. 5. Distribution of the wave speed in the main perforation along the samples' lengths at 177 Hz. Linear profile of Sample 3 (black) and modified profile of Sample 5 (grey). Both samples' are 75 mm long and maximum and minimum central perforation radii are 25 mm and 1 mm.
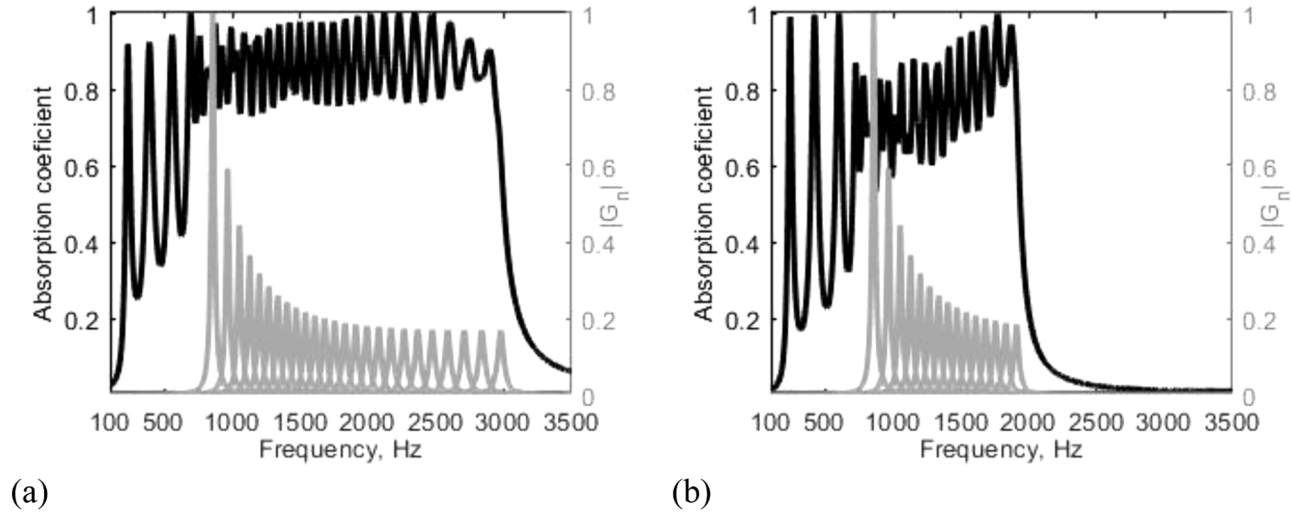
Fig. 6. Calculated absorption coefficient dependence on frequency (black, left y-axis) and absolute values of the normalised admittances of individual lateral cavities (grey, right y-axis). Calculations are performed using linear staircase $r(X)$ profile (23). Admittances are normalised by their maximum valuee (these correspond to cavities with the lowest resonance frequencies). a) Sample 1, L=100 mm. b) Sample 2, L=60 mm.

closest to the front surface and then reduces to a very low value. To demonstrate this effect, the results for Sample 2 are presented in Fig. 6,b, where the highest resonance frequency of the cavity is lower (due to a smaller hole radius of the front plate r_{max}, see Fig. 2,(a)). Hence, for this sample the frequency band where absorption coefficient stays high is narrower. As the minimum size of the orifice remains equal to 1 mm for both samples, the lowest resonance frequency of the cavities is the same for both samples and is close to 800 Hz.

For the frequencies higher than the resonance frequency of the plate closest to the front surface, the admittances of all cavities have larger imaginary part, then the real part. This can be easily understood if admittances of individual cavities as shown in Fig. 6 are approximated by the Lorenzian functions $G_i = \frac{i\omega\alpha_i}{\omega^2 - \omega_i^2 + i\omega\beta_i}$, where α_i and β_i are parameters determining the strength of the resonance and losses in a cavity number i. If $\omega \gg \max(\omega_i)$, then $G_i \approx \frac{i\alpha_i}{\omega}$. This means that the admittance of the main perforation wall defined by Eq. (16) is dominated by its imaginary part. As follows from equation (13), this means that the real part of the effective compressibility decreases and can become negative. Real part of the effective density remains positive as it does not depend on the admittances of the cavities. If one of the effective parameters of the equivalent medium has a negative real part, the waves can not propagate inside the material, i.e. bandgap is formed. The existence of the bandgap leads to almost full reflection of the wave from the surface of the absorber and hence an almost zero value of the absorption coefficient. To confirm this effect, real and imaginary parts of the effective compressibility $C_m(X)$ (equation (13)) are plotted for Sample 2 assuming frequency 3500 Hz in Fig. 7. At this frequency, as shown in Fig. 6,b, the absorption coefficient is very low The real part of the effective compressibility at this frequency is negative for all locations along the sample length, which means that no waves can propagate through the material.

Estimations confirm high absorption coefficient values at resonance frequencies of the side cavities, as shown in Fig. 6. To simplify the algebra, the cavities are treated as rigidly backed slits of length $R - r_i$, where r_i is the radius of perforation i. Using expressions (19) and (21) and condition of resonance $k_0(R - r_i)Re(\sqrt{\rho_c C_c}) = \frac{\pi}{2}$ of cavity i, the resonance frequency is estimated as $f_i = \frac{\omega_i}{2\pi} = \frac{c_0}{4(R - r_i)}\left(1 - \right.$

$\left. \left(1 + \frac{\gamma - 1}{\sqrt{N_{pr}}}\right)\sqrt{\frac{\eta(R - r_i)}{\pi c_0 \rho_0}}\frac{1}{d_c}\right)$. At this frequency the normalised admittance of the slit, can be estimated as $G(\omega_i) = i\cot(ik_0(R - r_i)Im(\sqrt{\rho_c(\omega_i)C_c(\omega_i)}))\sqrt{\frac{C_c(\omega_i)}{\rho_c(\omega_i)}} \approx \frac{c_0 d_c}{(R - r_i)\left(1 + \frac{\gamma - 1}{\sqrt{N_{pr}}}\right)}\sqrt{\frac{\rho_0}{\eta\pi f_i}}$. Here the expansions are performed assuming

$\sqrt{\frac{\eta(R - r_i)}{\pi c_0 \rho_0}}\frac{1}{d_c} \ll 1$, which is correct as $R - r_i \leq 50$ mm, and $d_c \geq 2$ mm.

Let's consider the front cavity of Sample 2 with $r_1 = 15$ mm. The resonance frequency of the slit of thickness $R - r_1 = 35$ mm is estimated as $f_i = 2.4$ kHz, while the numerical value for the annular cavity is 1.9 kHz. The normalised admittance of this cavity at resonance $G(\omega_1)$ is approximately equal to $58.3 \gg 1$. The resonance frequencies of the cavities with $i > 1$, situated closer to the backing, are lower than f_1, so the wave does not travel much further than the first section and the effective length of the sample can be estimated as $d_c + d_p$. The admittance of the wall of the section is $G_w = \frac{d_c}{d_p + d_c}G(\omega_1) \gg 1$. This means that, according to equation (13), $C_m \approx \frac{iG_w}{2k_0 r_1}\frac{r_1^2}{R^2}$. According to Eq. (12), $\rho_m \approx \frac{R^2}{r_1^2}$. Next, the input admittance of the sample is estimated: $\Gamma(\omega_1) = -i\tan(k_0(d_c + d_p)\sqrt{\rho_m C_m})$ $\sqrt{\frac{C_m}{\rho_m}} \approx -ik_0(d_c + d_p)C_m = G(\omega_1)\frac{d_c}{2r_1}\left(\frac{r_1}{R}\right)^2 \approx 0.53$. This value corresponds to absorption coefficient 0.90. Numerically obtained value of the absorption coefficient at the resonance frequency of the front cavity for Sample 2 is 0.97 (Fig. 6,b)

Below the frequency of the first cavity resonance, the absorption peaks are due to ``quarter wavelength'' resonances along the
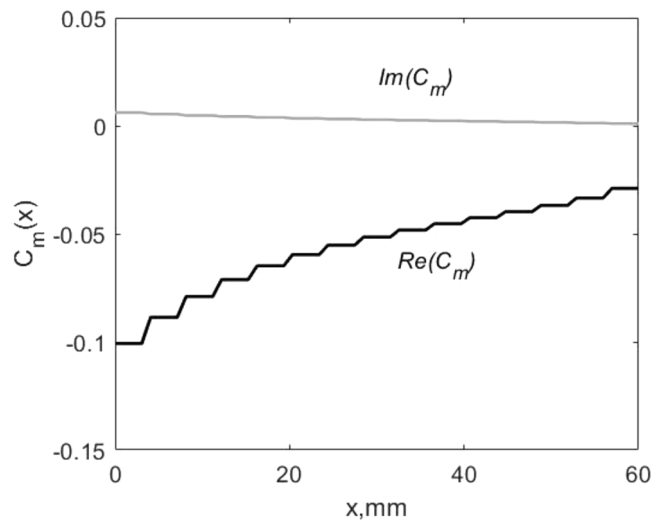

Fig. 7. Dependence of the normalised compressibility of the material along on the distance from the front surface at 3500 Hz. Linear profile of Sample 3. Real part – black line, imaginary part – grey line.
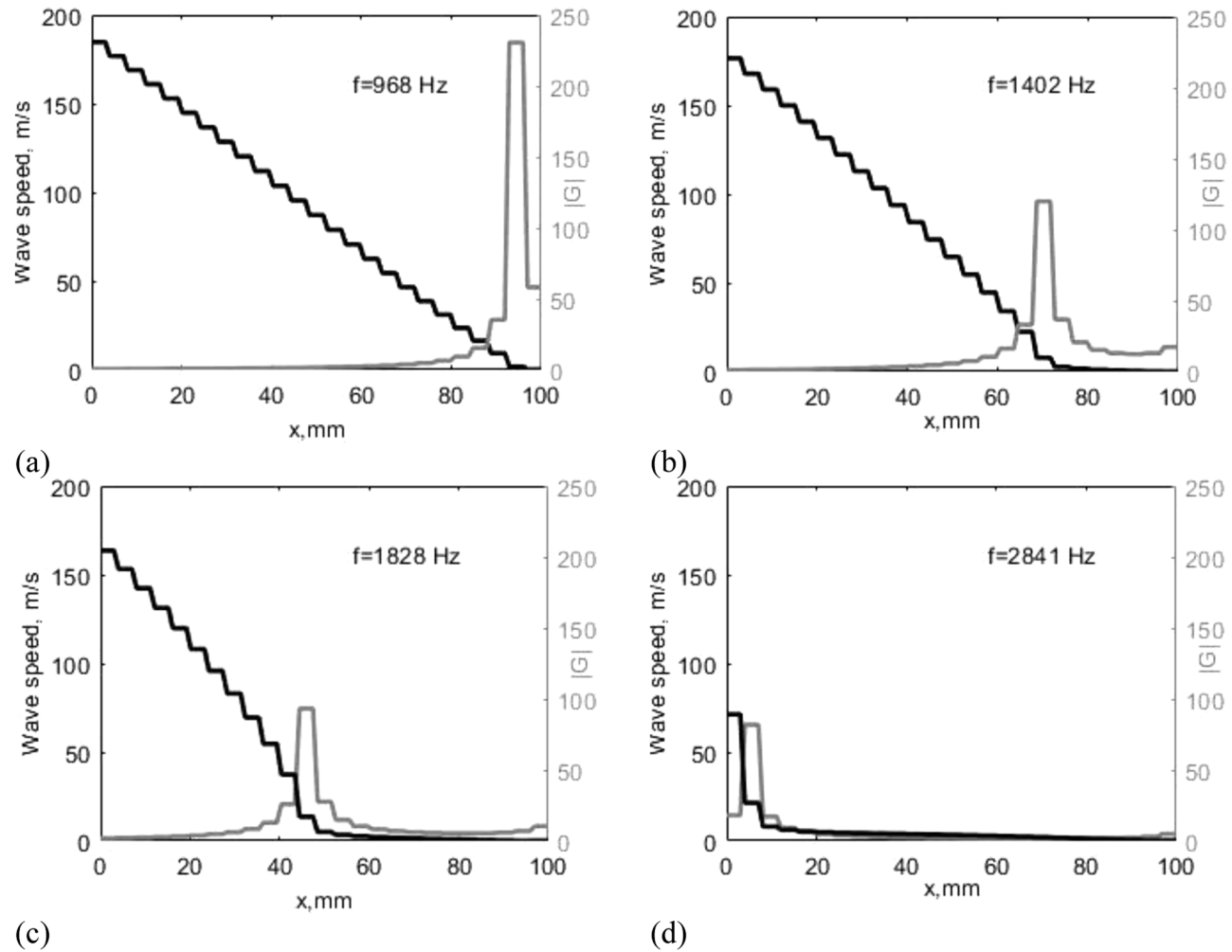
Fig. 8. Effect of the lateral cavities' resonances on the wave speed, Sample 1. Distribution of the wave speed in the main perforation along the sample length (left y-axis) and absolute values of the normalised wall admittance (16) (right y-axis).
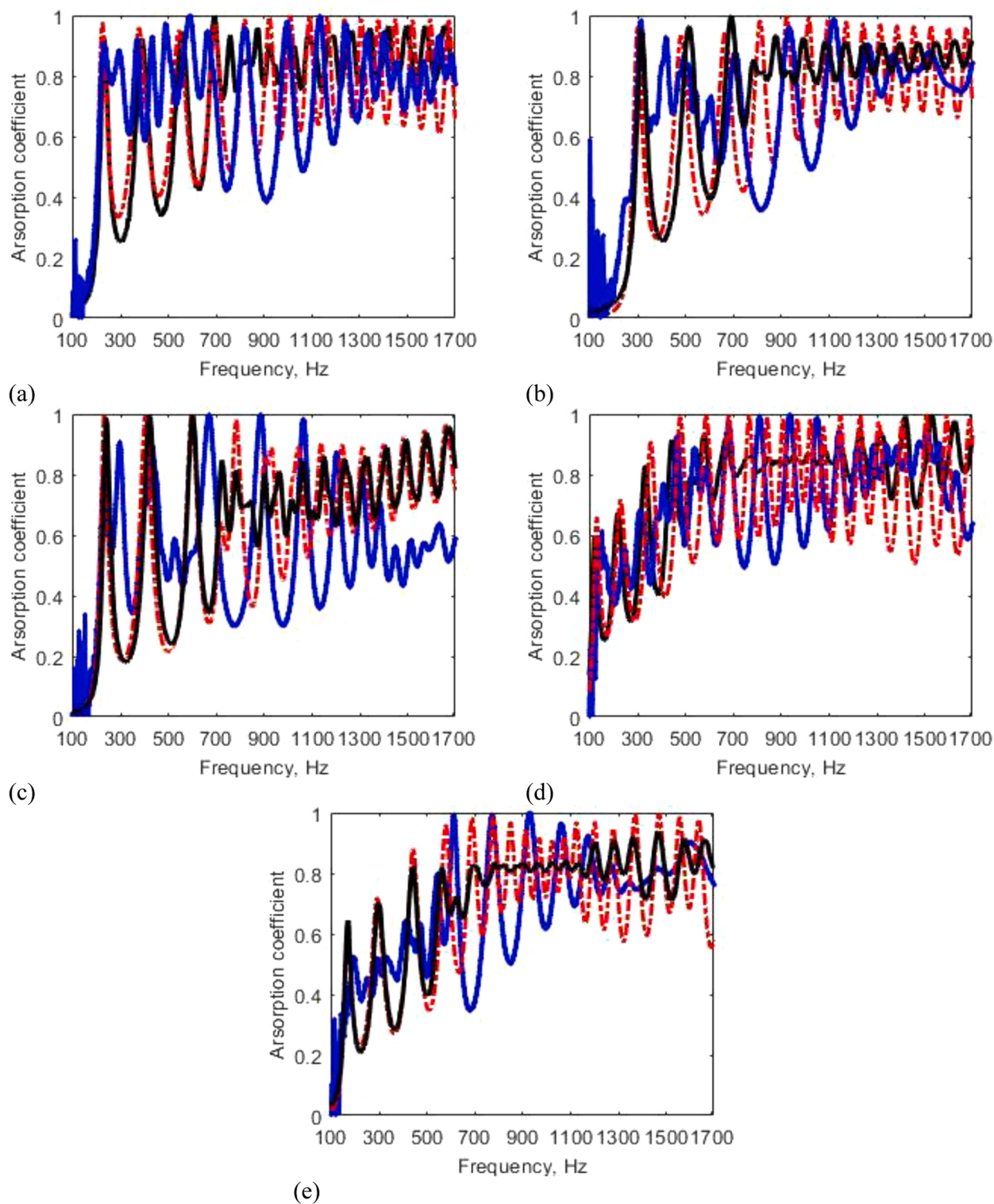
Fig. 9. Absorption coefficent dependence on frequency (colour online). Black solid lines – equivalent fluid model, red dash-dotted lines – FEM (rigid plates), blue markers – measurements. a-e Samples 1–5 respectively.

sample length. It is interesting to note, that although Sample 2 is 60 mm and Sample 1 is 100 mm in length, the frequencies of the first absorption peaks are not that different – 242 Hz for shorter sample and 231 Hz for a longer one. This illustrates the effect of the maximum orifice opening on the frequencies of the ``quarter wavelength resonances''. The wave speed averaged over the sample

length is lower for the sample with a smaller orifice radius at the front of the sample.

To summarise, high values of the absorption coefficient are sustained in the frequency range covering the resonances of the side cavities. This is because their resonance frequencies are close to each other (slight mistuning). The lower boundary of this frequency range is defined by the resonance frequency of the cavity closest to the backing, while the upper boundary corresponds to the resonance frequency of the cavity closest to the front surface of the absorber. The latter corresponds to higher frequency for the absorber with larger front opening (Fig. 6,a) and consequently smaller annular width of front cavity.

3.5. Effect of the lateral cavity resonances on sound speed variations along the sample length

As it is explained in [1], and illustrated in Fig. 5, the sound speed gradually decreases from the front surface of the sample and continues to do so until its rigid backing, where it becomes very close to zero. However, this is only true for the frequencies below the lowest cavity resonance. In Fig. 8,(a-d), the distributions of the wave speed and the modulus of the normalised wall admittance (16) along the length of Sample 1 are shown for different frequencies. The resonances of the individual cavities for this sample are shown in Fig. 6,(a). At the frequency $f = 968$ Hz, the resonance of the 24th cavity is observed. The cavities are counted from the front surface of the sample, which means the position of the 24th cavity is at $x = 93$ mm.

The wave speed reaches zero at the position, that corresponds to the maximum value of the admittance modulus, i.e. at the position of the 24th cavity. As the frequency increases, the cavities closer to the surface start resonating. At $f = 1402$ Hz (Fig. 8,(b)), 18th cavity which is located at $x = 69$ mm resonates. Wave speed remains very close to zero for all locations closer to the backing than this cavity, i.e. for $x > 69$ mm. At $f = 1828$ *Hz*, the resonance of cavity 12 located at $x = 45$ mm is achieved, and the sound does not propagate beyond this location (Fig. 8,(c)). And, finally, at frequency $f = 2841$ Hz, the 2nd cavity resonates and the sound barely penetrates the sample. This is shown in Fig. 8,(d). It could be noticed from Fig. 6,(a), that the sound absorption coefficient value remains large at this frequency, meaning that the energy loss is apparent inside the resonating cavity close to the surface of the sample.

For frequencies above the highest resonance frequency of the cavities (this corresponds to the cavity closest to the surface) the wave speed is effectively zero (however, its complex part is not) everywhere and nearly all incident energy is reflected from the sample, as discussed at the end of the previous section. The effects observed here are similar to that described in [12] for ``rainbow trapping absorber'', demonstrating ``trapping'' of sound at the location of resonating cavity. The arguments presented in Section 3.4 and illustrated in Fig. 7 are valid for the locations closer to the backing then the resonating cavity. This is because the resonance frequencies of the side-cavities at these locations are lower than that of the resonating cavity. This means that the effective compressibility of air positioned between the resonating cavity and the backing has negative real part and no propagating waves are supported.

4. Comparisons with FEM model and experiments

We validate the model by comparing its predictions with those of FEM model (commercial software COMSOL 5.4 is used) and the measurements. The latter are performed in B&K impedance tube using a standard 2 microphone method as outlined in [23]. The radius of the tube is 50 mm, so the samples are fitted tightly into the tube avoiding any gaps. The working frequency range of the experimental setup is 100–1700 Hz. First, the plates are modelled as perfectly rigid in COMSOL to allow the fair comparisons with the equivalent fluid model. A frequency domain model was created using Acoustics module in Comsol. Axial symmetry allowed to reduce the model to 2D geometry. Air in the main perforation and in the cavities is modelled as thermo-viscous fluid using Thermoviscous Acoustics interface, so no equivalent fluid assumptions are made in the numerical model. The maximum mesh element was ¼ of the plate thickness (0.25 mm) and the interactions between the fluid and the solid are considered using boundary layer feature of the mesh in COMSOL. We used triangular mesh elements and resolved eight boundary layers. A geometry of the impedance tube with incident plane wave was simulated in the model. Pressure values were calculated for two locations corresponding to positions of the microphones. After that the absorption coefficient was calculated following the method described in [23].

Comparisons of the absorption coefficients predicted by the semi analytical equivalent fluid model of Section 3, numerical finite element model and the data for all samples are shown in Fig. 8,(a-e). Equivalent fluid model and FEM give very close results at low frequencies, predicting matching values of absorption coefficient peaks. However, at higher frequencies the FEM model predicts oscillations of absorption coefficient (due to lateral cavity resonances) of a higher amplitude. This is likely to happen due to a) limited applicability of the equivalent fluid model for the portion of the sample where the central perforation radius becomes comparable to the lateral cavity width and b) due to possible interactions between the neighbouring cavities via evanescent waves. The former would mostly affect the range of frequencies which coincides with the resonances of the cavities close to the sample backing, where the central perforation radius becomes small (hence no scale separation). Indeed, the range around 1 kHz is where the differences between FEM and equivalent fluid models predictions are the most noticeable. The latter is not accounted at all in the equivalent fluid model, although could be taken into account in a model similar to [16]. Also, unlike [7], in the equivalent fluid model the end corrections of the side cavities are not accounted for. This is partially justified by the fact that the cavities' widths are much smaller than their depth making the contribution of end corrections relatively insignificant. Both models remain relatively close to the data in the low frequency range (exception is Sample 5, Fig. 8e). However, for most samples, the data shows absorption coefficient peaks that are not predicted by the models, e.g. see Fig. 9,(a) at low frequencies. Some peaks predicted by the model are not observed in the experiment, e.g. Fig. 9, (b) in the middle and higher frequency ranges. We believe that the imperfections of the mechanically built samples that were assembled in the laboratory might be the reason for this.

Overall, the agreement might be considered satisfactory. The experimental dependences of the absorption coefficient on frequency for all samples show peaks that are due to resonances along the sample length at low frequencies (global resonances) and those due to

resonances of the lateral cavities (local resonances). The samples are confirmed to show broadband absorption up to the frequencies of 1700 Hz. Obtaining data at higher frequencies was not possible for samples with the outer radius of 50 mm due to limitations of the plane wave approximation.

5. Effect of plate elasticity

It has been previously shown that the elasticity of the plates does influence the performance of the ``pancake'' absorbers, see [15, 24]. It is shown in Fig. 10, that for the absorbers with graded properties FEM predictions also change, when the plates are modelled as linear elastic material. The calculations have been performed for Sample 1 (Fig. 10,(a)) and Sample 4 (Fig. 10,(b)). Properties of aluminium have been used for modelling the plates. ``Clamped'' boundary condition was applied at the outer edge of the plates, while the inner edge was modelled as free boundary. Thermoviscous Acoustics interface was coupled with Solid Mechanics at the boundaries of the plates and air. Boundary layer feature of the mesh was still used to properly account for viscous and thermal losses at these boundaries. The size of the mesh was the same as for the case of perfectly rigid plates. The lowest resonance frequencies of the annular plates were calculated using FEM and varied from 1011 Hz for the plate nearest to the backing (shown with an arrow on Fig. 10,(a-b)) to 1753 Hz for the front plate with the central perforation radius of 25 mm. Taking elasticity of the plates into account does not
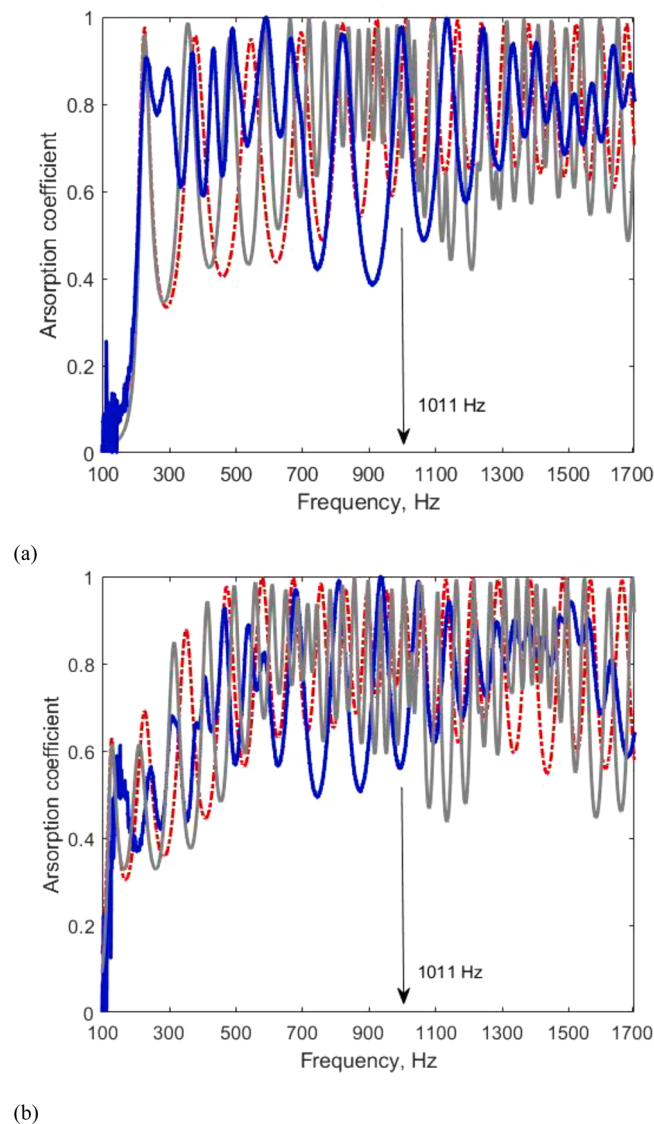

(a)

(b)

Fig. 10. Absorption coefficient predicted by FEM model with elastic plates and rigid plates. (colour online). Red dash-dotted lines – FEM predictions for rigid plates, grey solid lines – FEM predictions for elastic aluminium plates. Experimental results are shown with blue markers. a – Sample 1, b- Sample 4. Both samples have length 100 mm.

significantly improve the agreement with experiments. The most likely reason for this is inconsistency of the mounting conditions of the plates as the sample was assembled by hand. However, the model assuming elastic plates does predict high amplitude variations of the absorption coefficient in the frequency range of resonances of the plates with the smallest perforations (around 1000–1200 Hz). This is predicted for both samples. Similar behaviour is observed experimentally, but at slightly lower frequencies (around 750–1000 Hz). It was noted in [15] that in the experiment the boundary conditions were likely to be between ``simply supported'' and ``clamped''. The former produces lower resonance frequency. This, at least partially, explains the differences between the model predictions and the results of the experiments.

It is remarkable that the elasticity of the plates affects the absorption coefficient behaviour not just at higher frequencies where the resonances of the plates are expected to play a role, but also at much lower frequencies. Comparisons with measurements suggest that at low frequencies the frequencies of some peaks of the absorption coefficient are better predicted by the model with elastic plates. However, this is not a significant improvement and not valid for all peaks. For instance, the frequency of the second peak predicted for Sample 4 (Fig. 10,(b)) by the model with elastic plates is 208 Hz, whilst the model with the rigid plates predicts 224 Hz. In experiments, second absorption coefficient peak for this sample appears at 242 Hz. The peak absorption coefficient value is also affected by the plates' elasticity, where the model predicts 0.62 with elastic plates assumption and 0.69 with rigid plates. The measured value is 0.57. s This suggests that the plate elasticity has an effect on the wave speed profile. It should be noted that the resonance frequencies of the plates positioned close to the backing (small perforation radius) are close to the resonance frequencies of the cavities between them. For instance, for Sample 1, resonance frequency of the cavity 25, positioned next to the backing is 856 Hz (see Fig. 6,(a)), while the resonance frequency of the corresponding plate is 1011 Hz. The resonance of the preceding cavity 24 is given at 965 Hz, while the plate resonance remains at 1011 Hz still. And finally for the cavity 23, the resonance frequency is 1054 Hz and the plate resonance is predicted at 1012 Hz. Closer to the surface of the sample, the resonance frequencies of the cavities are higher but so are the resonance frequencies of the annular plates which have larger central orifice. This means, that a strong interplay between the resonances of different nature is likely to happen. Furthermore, in reference [24] it was shown that the vibration of the plates in the absorbers with a constant diameter perforation induce a vibrational bandgap effect around the first natural frequency of flexural vibrations. Within the bandgap, the absorption coefficient tends towards zero. In the ABH absorbers, however, the plates resonate at different frequencies and the effect of the vibrational bandgap is cancelled.

6. Conclusions

Acoustic structures with graded properties studied in this work could be described as multi-resonant absorbers. Their sound absorption performance is affected by the resonances a) along the sample length (quarter wavelength resonances or global resonances), b) cavity resonances and c) resonances of the elastic annular plates. The main result of this paper is the equivalent fluid model used for calculations of the surface impedance and consequently absorption coefficient of the structures with graded properties. Although this model is based on several crucial approximations, such as plane wave assumption and no interactions between the neighbouring lateral cavities, it is still able to predict the main features of the absorbers' performance and is easily adaptable to different designs.

The structures tested in this work are effective broad band absorbers. Their bandwidth is dependent on the length, front orifice radius compared to the sample radius and the distribution of cavity resonances. If the first cavity resonance is lower than the first resonance along the absorber length, then the former defines the lower boundary of the bandwidth, as in the work [12]. However, for the absorbers we studied, the bandwidth's lower boundary is defined by the quarter wavelength resonance along the sample length. This is because the absorbers are relatively long (60 mm to 1000 mm) and the lowest lateral cavity resonance was relatively high at around 900 Hz. The upper boundary of the bandwidth is defined by the highest resonance frequency of the lateral cavity. The model predicts that for the absorber with smaller front orifice radius (Sample 2) this boundary is at lower frequency, than for the absorber with larger front perforation but the same variations of the orifice radius along the length (e.g. Sample1). Testing this experimentally was not possible due to limitations of the experimental set-up and invalidity of plane wave approximation.

Sound speed inside the central perforation gradually decreases from the front surface of the sample towards its backing at low frequencies. The average value of the wave speed is responsible for the frequency of the absorption coefficient peak due to quarter wavelength resonance. The calculations predict a lower average wave speed for the horn type profile than for the linear profile of the central perforation. It has been demonstrated that at higher frequencies, the wave speed decreases along the sample length, ultimately reaching zero at different locations at different frequencies. These locations are defined by the cavity resonances.

Semi-analytical equivalent fluid model is found to be in a satisfactory agreement with FEM results, when rigid plates are assumed in the latter. This agreement is especially good at low frequencies. At higher frequencies, the validity of the equivalent fluid model is limited due to the lack of scale separation between the smallest sections of the central orifice and the lateral cavities' width.

The agreement between the models and the experiments is satisfactory for all five samples tested. The imperfections of the samples assembled by hand and their mounting conditions within the impedance tube are likely to be the reasons for the discrepancies between the data and the model predictions. Comparisons between the measurements and the model confirm that assumption of a smooth variations of the central perforation radius does not capture the oscillations of the absorption coefficent observed at higher frequencies. The performance of samples comprising 25 or less plates is affected by discrete nature of lateral cavity resonances, which is responsible for these variations.

Numerical calculations using COMSOL show that plate vibrations affect the absorber performance in the whole frequency range. Taking elasticity of the plate material into account results in the lower predicted frequencies of the absorption coefficient peaks. Furthermore, at higher frequencies the effect is the strongest for frequencies between 1000 and 1200 Hz. In this frequency range the resonances of the plates might interfere with the resonances of the lateral cavities bounded by them. The interplay of resonances of

different nature might be useful for the design of the graded absorbers and could form a basis of the future work. Alternatively, it might be possible to tune plate resonances in such a way that they interact with the resonances along the absorber length. It is also interesting to investigate the interaction between slightly mistuned resonances of neighbouring elastic plates.

The ABH sound absorbers studied in this work are lightweight, not fibrous and consequently nontoxic. With a relatively low thickness, they provide high sound absorption in a wide range of low and medium frequencies. What might be even more important, they can be used in harsh environments where conventional porous materials are not suitable. This includes environments with high temperature, high pressure, fluid flow. They could be used for example to reduce the noise of turbomachinery or rotating machines whose rotation speed can vary. They could find applications in airplane reactors, helicopter stators, automotive motors, air ducts, industrial chimneys, aerospace payload fairing, or protection system (Blast Suppression Dampers). It might also be possible to combine the ABH absorbers with conventional porous materials to widen the working frequency bandwidth

CRediT authorship contribution statement

Olga Umnova: Writing – original draft, Conceptualization, Methodology, Formal analysis, Supervision. **Daniel Brooke:** Writing – original draft, Methodology, Validation, Investigation. **Philippe Leclaire:** Writing – review & editing, Conceptualization, Methodology, Formal analysis, Supervision. **Thomas Dupont:** Writing – review & editing, Methodology, Formal analysis, Supervision.

Declaration of Competing Interest

None.

Data Availability

Data will be made available on request.

References

[1] M.A. Mironov, V.V. Pislyakov, One-dimensional acoustic waves in retarding structures with propagation velocity tending to zero, Acoust. Phys. 48 (2002) 347–352.
[2] V.V. Krylov, New type of vibration dampers utilising the effect of acoustic 'black holes", Acta Acust. 90 (2004) 830–837.
[3] A. Pelat, F. Gautier, S.C. Conlon, F. Semperlotti, The acoustic black hole: a review of theory and applications, J. Sound Vib. 476 (2020), 115316.
[4] A.A. El Ouahabi, V.V. Krylov, D.J. O'Boy, Experimental investigation of the acoustic black hole for sound absorption in air, in: The 22nd International Congress on Sound and Vibration, 2015. Florence, Italy 12-16 July.
[5] A.A. El Ouahabi, V.V. Krylov, D.J. O'Boy, Investigation of the acoustic black hole termination for sound waves propagating in cylindrical waveguides, in: Internoise 2015, 2015. San Francisco, California, USA 9-12 August.
[6] M. Mironov, V. Pislyakov, One-dimensional sonic black holes: exact analytical solution and experiments, J. Sound Vib. 473 (2020), 115223.
[7] O. Guasch, M. Arnela, P. Sanchez-Martin, Transfer matrices to calculate linear and quadratic acoustic black holes in duct terminations, J. Sound Vib. 395 (2017) 65–79.
[8] O. Guasch, P. Sanchez-Martin, D. Ghilardi, Application of the transfer matrix approximation for wave propagation in a metafluid representing an acoustic black hole duct termination, Appl. Math. Model. 77 (2020) 1881–1893.
[9] Y. Mi, W. Zhai, L. Cheng, C. Xi, X. Yu, Wave trapping by acoustic black hole: simultaneous reduction of sound reflection and transmission, Appl. Phys. Lett. 118 (2021), 114101.
[10] J.P. Hollkamp, F. Semperlotti, Application of fractional order operators to the simulation of ducts with acoustic black hole terminations, J. Sound Vib. 465 (2020), 115035.
[11] Z. Xiaoqi, C. Li, Broadband and low frequency sound absorption by sonic black holes with micro-perforated boundaries, J. Sound Vib. 512 (2021), 116401.
[12] N. Jiménez, V. Romero-García, V. Pagneux, J.-.P. Groby, Rainbow-trapping absorbers: broadband, perfect and asymmetric sound absorption by subwavelength panels for transmission problems, Sci. Rep. 7 (2017) 13595.
[13] A. Mousavi, M. Berggren, E. Wadbro, How the waveguide acoustic black hole works: a study of possible damping mechanisms, J. Acoust. Soc. Am. 151 (2022) 4279–4290.
[14] M. Cervenka, M. Bednarik, On the role of resonance and thermoviscous losses in an implementation of "acoustic black hole" for sound absorption in air, Wave Motion 114 (2022), 103039.
[15] D.C. Brooke, O. Umnova, P. Leclaire, T. Dupont, Acoustic metamaterial for low frequency sound absorption in linear and nonlinear regimes, J. Sound Vib. 485 (2020), 115585.
[16] J.F. Allard, N. Atalla, Propagation of Sound in Porous Media: Modelling Sound Absorbing Materials, 2nd ed., John Wiley & Sons, New York, 2009, pp. 74–90. Ch. 5.
[17] L.E. Kinsler, A.R. Frey, A.B. Coppen, J.V. Sanders, Fundamentals of Acoustics, 4th ed., John Wiley & Sons, New York, 2000, p. 414.
[18] E. von Kamke, Differentialgleichungen, Springer, Fachmedien Wiesbaden, 1977, p. 21 (in German).
[19] P. Leclaire, O. Umnova, T. Dupont, R. Panneton, Acoustical properties of air-saturated porous material with periodically distributed dead-end pores, J. Acoust. Soc. Am. 137 (2015) 1772–1782.
[20] J.-.P. Groby, W. Huang, A. Lardeau, Y. Auregan, The use of slow waves to design simple sound absorbing materials, J. Appl. Phys. 117 (2015), 124903.
[21] H. Tijdeman, On the propagation of sound waves in cylindrical tubes, J. Sound Vib. 39 (1975) 1–33.
[22] X. Olny, C. Boutin, Acoustic wave propagation in double porosity media, J. Acoust. Soc. Am. 114 (2003) 73–89.
[23] ISO 10534-2, Acoustics—Determination of Sound Absorption Coefficient and Impedance in Impedance tubes. Part 2: Transfer-Function Method, International Organization for Standardization, Geneva, Switzerland, 1998.
[24] T. Dupont, P. Leclaire, R. Panneton, O. Umnova, A microstructure material design for low frequency sound absorption, Appl. Acoust. 136 (2018) 86–93.